






Cite this: *RSC Adv.*, 2021, 11, 34152

# Effect of porous structural properties on lithium-ion and sodium-ion storage: illustrated by the example of a micro-mesoporous graphene<sub>1-x</sub>(MoS<sub>2</sub>)<sub>x</sub> anode

Yige Sun, <sup>†\*ab</sup> Jie Tang, <sup>\*ab</sup> Kun Zhang, <sup>a</sup> Xiaoliang Yu,<sup>a</sup> Jinshi Yuan,<sup>a</sup> Da-Ming Zhu,<sup>c</sup> Kiyoshi Ozawa<sup>a</sup> and Lu-Chang Qin <sup>d</sup>

In this work, we synthesized micro-mesoporous graphene<sub>1-x</sub>(MoS<sub>2</sub>)<sub>x</sub> with different compositional ratios via co-reduction of graphite oxide and exfoliated MoS<sub>2</sub> platelets. We systematically studied the performance of the micro-mesoporous graphene<sub>1-x</sub>(MoS<sub>2</sub>)<sub>x</sub> as anodes in lithium-ion batteries and sodium-ion batteries. The results show that the specific surface areas of the composites decrease with introducing MoS<sub>2</sub>. The irreversible capacitance, which is related to the formation of solid electrolyte interphases, also decreases. Besides specific surface area, we found that micropores can benefit the lithiation and sodiation. We demonstrated that a specific charge capacity of 1319.02 mA h g<sup>-1</sup> can be achieved at the 50th cycle for the graphene<sub>2/3</sub>(MoS<sub>2</sub>)<sub>1/3</sub> anode in lithium-ion batteries. Possible relationships between such a high specific capacity and the micro-mesoporous structure of the graphene<sub>1-x</sub>(MoS<sub>2</sub>)<sub>x</sub> anode are discussed. This work may shed light on a general strategy for the structural design of electrode materials in lithium-ion batteries and sodium-ion batteries.

Received 5th July 2021  
Accepted 12th October 2021

DOI: 10.1039/d1ra05179b

rsc.li/rsc-advances

## 1. Introduction

Lithium-ion batteries (LIBs) with high energy density have enjoyed great success recently.<sup>1,2</sup> Extensive work has been carried out toward continued improvements of the capacity, the life span, and the safety of LIBs in the past decade.<sup>3-5</sup> One of the approaches used in the improvement of the capacity is to employ new electrode materials with porous structures.<sup>6-8</sup>

There are both advantages and disadvantages of applying a porous structure in an electrode material. The advantages include: (i) reduced solid-state diffusion of Li-ions due to thin pore walls, (ii) good electrode-electrolyte contact due to the high surface area, (iii) fast Li-ion diffusion kinetics, and good rate capability due to hierarchical structures of pores. For example, the micropores in low-temperature carbons (LTCs) below 100 nm are believed to act as the “reservoirs” for lithium

storage.<sup>9</sup> Ordered multimodal porous carbons, with a specific surface area of 1120 m<sup>2</sup> g<sup>-1</sup>, exhibit a reversible capacity of 903 mA h g<sup>-1</sup> and high rate performance, due to facile penetration of the porous structure.<sup>10</sup> However, a porous structure has several disadvantages, such as poor cycle stability due to the instability of such a structure,<sup>9,11</sup> and high irreversible capacity due to excessive solid electrolyte interphase (SEI) formation.<sup>12</sup> Porous structural properties, including specific surface area, pore size, pore distribution, and so forth, form an integrated system, which plays a crucial role in lithium-ion storage.

Different electrode materials require different porosity designs. For LiMnPO<sub>4</sub>/C, the reversible capacity is proportional to specific surface area and pore volume, due to more active sites contacted with electrolyte ions.<sup>13</sup> However, the capacity of a lithium storage device is not proportional to pore size. Graphite with a low specific surface area was believed to be a suitable electroactive material.<sup>14</sup> In ordered mesoporous carbons, mesoporous contribute more than microporous.<sup>15</sup> While phosphorus@carbon benefits from the pores smaller than 1 nm, which play a crucial role in bond formation between phosphorus and carbon.<sup>16</sup> There are also different studies on CNT-Carbon nanofibers<sup>17</sup> and LiFePO<sub>4</sub>/C.<sup>18</sup> One reason for such a significant difference is the different nature and geometry of various materials. This suggests the need for careful analysis of the influence of surface properties on electrochemistry of different electrode materials.

<sup>a</sup>National Institute for Materials Science, 1-2-1 Sengen, Tsukuba 305-0047, Japan. E-mail: tang.jie@nims.go.jp

<sup>b</sup>Doctoral Program in Materials Science and Engineering, University of Tsukuba, 1-1-1 Tennodai, Tsukuba 305-8577, Japan

<sup>c</sup>Department of Physics and Astronomy, University of Missouri-Kansas City, Kansas City, Missouri 64110, USA

<sup>d</sup>Department of Physics and Astronomy, University of North Carolina at Chapel Hill, Chapel Hill, NC 27599-3255, USA

<sup>†</sup> Current address: Department of Materials, University of Oxford, Parks Road, Oxford OX1 3PH, UK; The Faraday Institution, Quad One, Harwell Science and Innovation Campus, Didcot OX11 0RA, UK.



There have been very few such investigations on graphene/molybdenum disulfide ( $\text{graphene}_{1-x}(\text{MoS}_2)_x$ ) anode.  $\text{Graphene}_{1-x}(\text{MoS}_2)_x$  is combined by two kinds of layered material. In which,  $\text{MoS}_2$  is a newly developed material.<sup>19</sup> In a  $\text{MoS}_2$  crystal, each Mo atom and S atom are covalently bonded forming a two-dimensional (2D) layered structure. These 2D layers are stacked together through weak van der Waals attraction, providing a very large interlayer spacing of about 0.61 nm along the *C*-axis.<sup>20,21</sup> This interlayer spacing is about twice that of graphite (0.335 nm). Therefore,  $\text{MoS}_2$  can easily accommodate lithium-ions and sodium-ions.<sup>22–24</sup>  $\text{MoS}_2$  has a theoretical specific capacity of  $670 \text{ mA h g}^{-1}$  in lithium-ion batteries. However, the low conductivity, layer restacking, low cyclic stability, and low rate performance are the key issues that limit the application of  $\text{MoS}_2$  as materials for constructing LIB's anodes. To solve the problem, carbon material, such as graphene, was used as binders and "skeleton" in a  $\text{MoS}_2$ . Such graphene could be produced by expanding graphite flakes at low cost and high throughput.<sup>25</sup> This  $\text{graphene}_{1-x}(\text{MoS}_2)_x$  anode can achieve a capacity of  $877 \text{ mA h g}^{-1}$  at a current density of  $100 \text{ mA g}^{-1}$ .<sup>26</sup> Although considerable research has been devoted to increasing the specific capacity, rather less attention has been paid to understand how porous structural properties affect electrochemistry performance of  $\text{graphene}_{1-x}(\text{MoS}_2)_x$ .

To our best knowledge, no experimental study has been reported which details the effects of porosity structure in  $\text{graphene}_{1-x}(\text{MoS}_2)_x$  on the electrochemical performance as anodes in LIBs and sodium-ion batteries (SIBs). In this work, by using reduced graphite oxide, we synthesized micro-mesoporous  $\text{graphene}_{1-x}(\text{MoS}_2)_x$  composite with increased specific surface area and similar pore-size distribution. We analyzed the effect of specific surface area and pore size distribution of micro-mesoporous  $\text{graphene}_{1-x}(\text{MoS}_2)_x$  anodes. The results suggest that instead of specific surface area, the pores with a radius smaller than 2 nm play an important role in the kinetics of both lithium-ion and sodium-ion storage. The results of this work may shed light on the application of  $\text{graphene}_{1-x}(\text{MoS}_2)_x$  in lithium-ion and sodium-ion storage devices. The discussion of porous structural properties and their effect on lithium-ion/sodium-ion storage may benefit the structural design of other electrodes.

## 2. Experimental

### 2.1 Synthesis of micro-mesoporous $\text{graphene}_{1-x}(\text{MoS}_2)_x$

To synthesize micro-mesoporous  $\text{graphene}_{1-x}(\text{MoS}_2)_x$ , bulk  $\text{MoS}_2$  was dispersed in a solvent containing  $\text{H}_2\text{O}_2$  (30 wt% aqueous solution) and *N*-methyl-2-pyrrolidinone (NMP) (1 : 9 v/v), followed by subsequently sonication (with a nominal power of 500 W) at room temperature for 12 hours to produce exfoliated  $\text{MoS}_2$  platelet. Then, graphite oxide dispersion ( $0.5 \text{ mg mL}^{-1}$ ) was synthesized through the modified Hummers' method as discussed in our previous work.<sup>27,28</sup> To form the micro-mesoporous  $\text{graphene}_{1-x}(\text{MoS}_2)_x$ , graphite oxide dispersion was mixed with as-prepared  $\text{MoS}_2$  platelet dispersion with different weight ratios (weight ratio of reduced graphite oxide to

$\text{MoS}_2$ ) of 1 : 0.2, 1 : 0.5, 1 : 1, 1 : 3, and 1 : 5. Then, hydrazine monohydrate (3  $\mu\text{L}$  for 3 mg graphite oxide) was added to the mixture, followed by reflux at  $98^\circ\text{C}$  for 24 hours. The product  $\text{graphene}_{1-x}(\text{MoS}_2)_x$  with different weight ratios were labeled as  $\text{Graphene}_{\frac{5}{6}}(\text{MoS}_2)_{\frac{1}{6}}$ ,  $\text{Graphene}_{\frac{2}{3}}(\text{MoS}_2)_{\frac{1}{3}}$ ,  $\text{Graphene}_{\frac{1}{2}}(\text{MoS}_2)_{\frac{1}{2}}$ ,  $\text{Graphene}_{\frac{1}{3}}(\text{MoS}_2)_{\frac{2}{3}}$ , and  $\text{Graphene}_{\frac{1}{6}}(\text{MoS}_2)_{\frac{5}{6}}$  respectively. The samples, in form of black power, were filtered and washed by using distilled water 5 times until the pH reached 7.

### 2.2 Fabrication of $\text{graphene}_{1-x}(\text{MoS}_2)_x$ electrode

$\text{Graphene}_{1-x}(\text{MoS}_2)_x$  powders were dispersed in ethanol to form a suspension, and then filtered through a weighted porous filter membrane (47 mm hydrophilic PTFE membrane filter,  $0.2 \mu\text{m}$  pore size, Merck Millipore). The membranes which contain  $\text{graphene}_{1-x}(\text{MoS}_2)_x$  powders were dried in a vacuum for 24 hours to remove water and ethanol, followed by cutting into 15 mm diameter circular disks. The circular disks were dried in a vacuum at  $110^\circ\text{C}$  for 12 hours, which were used as the electrodes in CR2032-type coin cells.

### 2.3 Structural characterization

The surface morphologies of samples were examined using a scanning electron microscope (SEM) and high-resolution transmission electron microscopy (HRTEM). The microscopic structures were characterized through X-ray diffraction (XRD, Rigaku SmartLab using  $\text{Cu K}\alpha$  radiation with  $\lambda = 1.5418 \text{ \AA}$ ). Elemental mapping (Energy dispersive X-ray spectroscopy-EDS) was performed by using a JEOL JSM-7100F instrument.

### 2.4 Adsorption isotherm characterization

Nitrogen adsorption measurements were performed by using Autosorb-1 (Quantachrome Instruments) at  $-196^\circ\text{C}$ . Samples were outgassed at  $150^\circ\text{C}$  for 24 hours before  $\text{N}_2$  adsorption. To calculate the specific surface area, the Brunauer–Emmett–Teller (BET) equation was used. Taking the porosity and surface energy of the solid into account, we used Density Functional Theory (DFT) model (from Quantachrome Autosorb ASiQwin 2.0) to analyze the pore size distributions.

### 2.5 Electrochemical performance

The electrochemical properties of the  $\text{graphene}_{1-x}(\text{MoS}_2)_x$  electrodes were characterized by assembling them in CR2032-type coin cells. The lithium foil acted as a reference and a counter electrode. A piece of polypropylene was used as the separator, and  $\text{LiPF}_6$  ( $1 \text{ mol L}^{-1}$  in EC : DMC = 1 : 1 (v/v %)) was used as the electrolyte to assemble LIBs. To assemble SIBs, a piece of sodium foil and  $\text{NaPF}_6$  electrolyte ( $1 \text{ mol L}^{-1}$  in EC : DMC = 1 : 1 (v/v %)) were used to replace lithium foil and  $\text{LiPF}_6$  electrolyte. The cells were galvanostatically charged and discharged under increasing current densities to evaluate the rate performance. Cyclic voltammetry measurements were carried out at a potential scan rate of  $0.1 \text{ mV s}^{-1}$ .



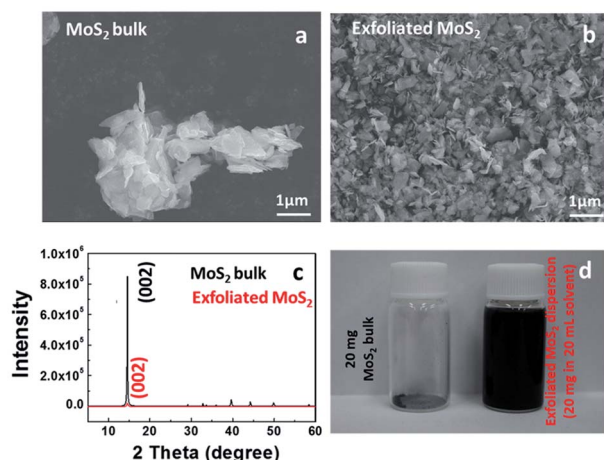


Fig. 1 Scanning electron microscopy (SEM) image of (a) MoS<sub>2</sub> bulk and (b) exfoliated MoS<sub>2</sub>. (c) X-ray diffraction patterns of MoS<sub>2</sub> bulk and exfoliated MoS<sub>2</sub>. (d) Photographs of MoS<sub>2</sub> bulk and exfoliated MoS<sub>2</sub> dispersions.

## 2.6 Li<sup>+</sup>/Na<sup>+</sup> diffusion coefficient calculation

To analyze the influence of surface properties on the lithium-ion and sodium-ion storage kinetics, electrochemical impedance spectroscopy (EIS) measurements at a 50% state of charge (SOC) in an AC frequency (from 200 kHz to 0.01 Hz) was carried out using a Biologic VMP-3 model. The lithium-ion and sodium-ion diffusion coefficient  $D$  was calculated using eqn (1):<sup>13,29,30</sup>

$$D = \frac{R^2 T^2}{2A^2 n^4 F^4 C^2 \sigma^2} \quad (1)$$

where  $R$  is the gas constant ( $8.314 \text{ J K}^{-1} \text{ mol}^{-1}$ ),  $T$  is the absolute temperature,  $A$  is the surface area of a electrode ( $A = \text{specific surface area} \times \text{mass of active electrodes}$ ),  $n$  is the number of transferred electrons,  $F$  is the Faraday's constant ( $96500 \text{ C mol}^{-1}$ ),  $C$  is the concentration of lithium-ion or sodium-ion,  $\sigma$  is the Warburg factor (the slope of line  $Z' \sim \omega^{-1/2}$  as shown in Fig. 6b and 8b).

## 3. Results and discussion

### 3.1 Structure characterization and morphology

Fig. 1 illustrates SEM images and XRD patterns of bulk MoS<sub>2</sub> and exfoliated MoS<sub>2</sub>. Compared with bulk particles in Fig. 1a, the exfoliated MoS<sub>2</sub> sheets in Fig. 1b exhibited a wider lateral size distribution. After sonication, the MoS<sub>2</sub> sheets were peeled off from the bulk particles, due to the weak van der Waals force.<sup>20</sup> Before exfoliation, the XRD spectrum of the bulk MoS<sub>2</sub> shown a (002) peak at  $14.51^\circ$  (Fig. 1c), indicating a  $d_{002}$  of 0.61 nm. After exfoliation, the absolute intensity of the (002) peak decreased dramatically, indicating the lower degrees of periodicity on the (002) face due to the exfoliation. Through the exfoliation process, we produced MoS<sub>2</sub> sheets from large particles as shown in Fig. 1d.

SEM images in Fig. 2 illustrate the morphology of the sample *Graphene<sub>2</sub>(MoS<sub>2</sub>)<sub>3</sub>*. The distributions of sulfur, carbon, and molybdenum were detected by EDS elemental mapping in Fig. 2b–d. It could be seen that the graphene and MoS<sub>2</sub> sheet were mixed together in *Graphene<sub>2</sub>(MoS<sub>2</sub>)<sub>3</sub>* composite in the high-resolution transmission electron microscopy image in Fig. 2e. Fig. 2f and g show the intensity profiles along the red line (reduced graphite oxide: graphene) and orange line (exfoliated MoS<sub>2</sub>) in Fig. 2e respectively. For graphene, the average distance between neighboring sheets was 0.37 nm, which was consistent with that in our previous report.<sup>27</sup> For exfoliated MoS<sub>2</sub> sheet, the interlayer spacing was 0.61 nm. This inter-layer spacing was in good agreement with the XRD pattern in Fig. 1c.

### 3.2 Effect of specific surface area on lithium storage

As shown in Fig. 3a, the exfoliate MoS<sub>2</sub> exhibited a type II isotherm with a specific surface area of only  $17 \text{ m}^2 \text{ g}^{-1}$ . The absence of hysteresis indicated adsorption on and desorption from a macro-porous or a non-porous surface.<sup>31</sup> In contrast, *Graphene<sub>2</sub>(MoS<sub>2</sub>)<sub>3</sub>* in Fig. 3b exhibited a type IV isotherm (specific surface area of  $321 \text{ m}^2 \text{ g}^{-1}$ ). The hysteresis indicated capillary condensation in mesopores. The closure at  $P/P_0$

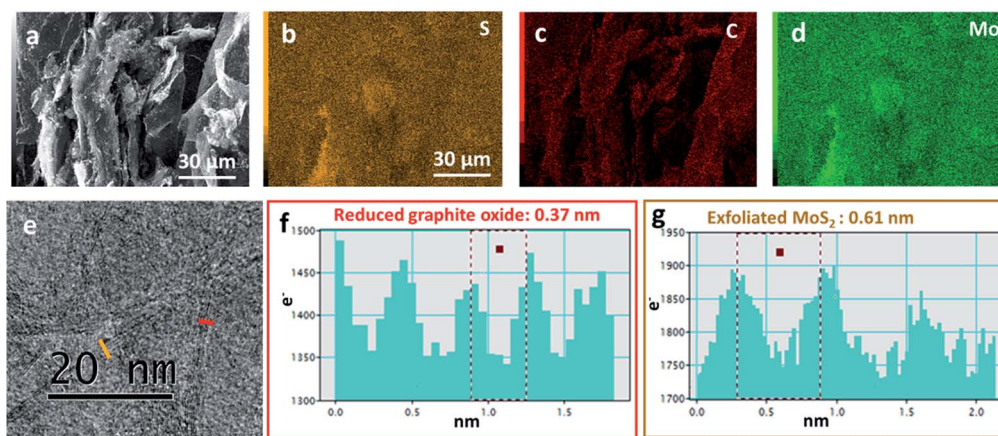


Fig. 2 (a) Scanning electron microscopy (SEM) image of *Graphene<sub>2</sub>(MoS<sub>2</sub>)<sub>3</sub>*. (b–d) The corresponding energy dispersive X-ray spectroscopy-EDS mapping images of sulfur, carbon, and molybdenum elements. (e) High-resolution transmission electron microscopy (HRTEM) image of *Graphene<sub>2</sub>(MoS<sub>2</sub>)<sub>3</sub>*. (f) and (g) Line profile of (e).





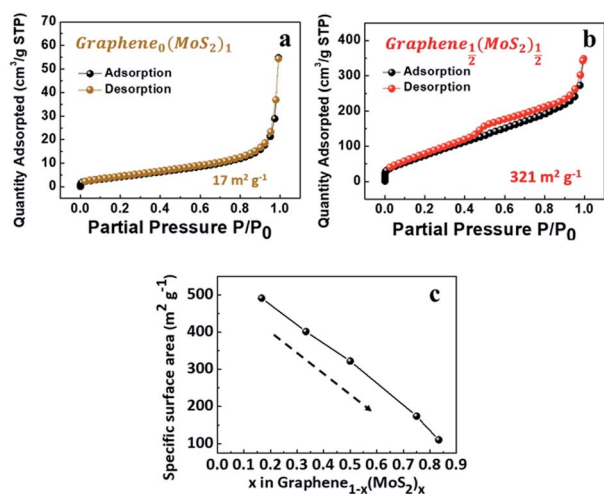


Fig. 3 Nitrogen physisorption isotherms of (a) exfoliated  $\text{MoS}_2$ , and (b)  $\text{Graphene}_{1/2}(\text{MoS}_2)_{1/2}$ . (c) Specific surface area as a function of  $x$  in  $\text{Graphene}_{1-x}(\text{MoS}_2)_x$  (weight ratio).

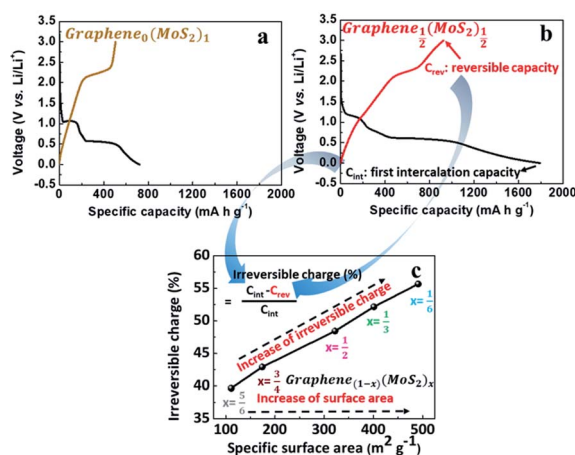


Fig. 4 First galvanostatic charge/discharge cycle of (a) exfoliated  $\text{MoS}_2$  and (b)  $\text{Graphene}_{1/2}(\text{MoS}_2)_{1/2}$  at  $50 \text{ mA g}^{-1}$  in  $\text{LiPF}_6$  (1 mol  $\text{L}^{-1}$  in EC : DMC = 1 : 1 (v/v %)) electrolyte. (c) Irreversible charge consumption in the first cycle as a function of the specific surface area.

around 0.45 indicated the presence of small mesopores, due to the tensile strength effect (TSE) as discussed by Groen *et al.*<sup>32</sup>

With the decrease of  $\text{MoS}_2$  amount, the specific surface area was increased from  $111 \text{ m}^2 \text{ g}^{-1}$  ( $\text{Graphene}_{1/6}(\text{MoS}_2)_{1/6}$ ) to  $491 \text{ m}^2 \text{ g}^{-1}$

for ( $\text{Graphene}_{5/6}(\text{MoS}_2)_{1/6}$ ) as shown in Fig. 3c. This was because excessive  $\text{MoS}_2$  flakes tend to restack together and decrease the surface area.<sup>20</sup>

Fig. 4a and b are the first galvanostatic charge and discharge curves of exfoliated  $\text{MoS}_2$  ( $\text{Graphene}_0(\text{MoS}_2)_1$ ) and  $\text{Graphene}_{1/2}(\text{MoS}_2)_{1/2}$ . In the intercalation curve, there were two typical plateaus indicating the formation of  $\text{Li}_x\text{MoS}_2$  around 1.1 V (vs.  $\text{Li/Li}^+$ ) and that of  $\text{Li}_2\text{S}$  around 0.6 V (vs.  $\text{Li/Li}^+$ ).<sup>33</sup>  $\text{Graphene}_{1/2}(\text{MoS}_2)_{1/2}$  exhibited much higher specific capacity compared with that of  $\text{Graphene}_0(\text{MoS}_2)_1$ . The first intercalation capacity of  $\text{Graphene}_{1/2}(\text{MoS}_2)_{1/2}$  was  $1792.47 \text{ mA h g}^{-1}$  (vs.  $721.52 \text{ mA h g}^{-1}$  for  $\text{Graphene}_0(\text{MoS}_2)_1$ ). The first reversible capacity was  $924.64 \text{ mA h g}^{-1}$  (vs.  $505.35 \text{ mA h g}^{-1}$  for exfoliated  $\text{MoS}_2$ ). This increase was due to the micro-mesopore structure of  $\text{Graphene}_{1-x}(\text{MoS}_2)_x$  which could provide better delivery of ions and increased conductivity.<sup>6,8</sup> As shown in Fig. 4c and Table 1, an increase of specific surface area lead to a dramatic increase of irreversible charge in the first cycle. The irreversible charge ratio was calculated by the eqn (2):<sup>12,14</sup>

$$\text{Irreversible charge ratio} = \frac{C_{\text{int}} - C_{\text{rev}}}{C_{\text{int}}} \times 100\% \quad (2)$$

in which  $C_{\text{int}}$  is the specific capacity in the first lithium-ion intercalation as shown in Fig. 4b,  $C_{\text{rev}}$  is the reversible specific capacity during the lithium-ions de-intercalation.

This irreversible charge is due to the formation of a solid electrolyte interphase (SEI). It is generally accepted that the formation of SEI consumes the lithium-ions during the intercalation on all the surface areas exposed to the electrolyte.<sup>8,12</sup> Therefore, the irreversible charge greatly depends on the specific surface area of the electrode. As shown in Fig. 4c, the irreversible charge in the first cycle was plotted as a linear function of the specific surface areas. This result was consistent with a previous study on graphite anode.<sup>12</sup> To note that to achieve the complete formation of the SEI layer and maximize the irreversible capacity in the experiment, we chose a small current density of  $50 \text{ mA g}^{-1}$  at room temperature for galvanostatic charge and discharge. Due to the effect of specific surface area on the irreversible charge,  $\text{Graphene}_{1/6}(\text{MoS}_2)_{1/6}$  seems to show a better performance in lithium storage. However, the diffusion study showed that tendency of lithium-ions diffusion kinetics was different, as the following discussion in Section 3.4.

Table 1 Nitrogen physisorption data and kinetic parameters of  $\text{Graphene}_{1-x}(\text{MoS}_2)_x$  electrodes in lithium-ion batteries and sodium-ion batteries<sup>a</sup>

Samples, $\text{Graphene}_{1-x}(\text{MoS}_2)_x$	$S_{\text{BET}}$	Irreversible charge in 1st cycle	$R_{\text{ct}} (\text{Li}^+)$	$D_{\text{Li}^+}$	$R_{\text{ct}} (\text{Na}^+)$	$D_{\text{Na}^+}$	Pore size (nm)
$\text{Graphene}_{5/6}(\text{MoS}_2)_{1/6}$	491	56%	90.23	3.73	111.68	5.21	3.7
$\text{Graphene}_{4/5}(\text{MoS}_2)_{1/5}$	401	52%	68.79	4.81	90.42	7.92	3.7
$\text{Graphene}_{3/4}(\text{MoS}_2)_{1/4}$	322	48%	48.90	5.70	76.27	9.15	3.7
$\text{Graphene}_{2/3}(\text{MoS}_2)_{1/3}$	174	43%	125.59	3.13	133.12	2.66	3.7
$\text{Graphene}_{1/2}(\text{MoS}_2)_{1/2}$	111	39%	223.02	0.24	249.53	0.31	3.7

<sup>a</sup>  $S_{\text{BET}}$ : specific BET surface area ( $\text{m}^2 \text{ g}^{-1}$ ),  $R_{\text{ct}}$ : charge-transfer resistance ( $\Omega$ ),  $D_{\text{Li}^+}$ : lithium-ions diffusion coefficient ( $\times 10^{-11} \text{ cm}^2 \text{ s}^{-1}$ ),  $D_{\text{Na}^+}$ : sodium-ions diffusion coefficient ( $\times 10^{-12} \text{ cm}^2 \text{ s}^{-1}$ ).



### 3.3 Pore size distribution

For a better characterizing of porous structural properties, differential-porosity measurements were performed. The pore size distributions are shown in Fig. 5. The pore-size distributions obtained with the porosity model indicated the micro-mesopore structure of  $\text{graphene}_{1-x}(\text{MoS}_2)_x$  samples. The main pore size was 3.7 nm, which was like the pore size of graphene (reduced graphite oxide) as discussed in our previous report.<sup>27</sup> The DFT porosity calculation results indicated that for  $\text{Graphene}_1(\text{MoS}_2)_5$  and  $\text{Graphene}_1(\text{MoS}_2)_4$  (Fig. 5a and b), most of the pores were bigger than 2 nm, since  $\text{MoS}_2$  flakes were dominant in these two samples. With the decrease of  $\text{MoS}_2$ , there were more contact points between graphene and  $\text{MoS}_2$  flakes, resulting in a fuller combination, and then formed more micropores between the graphene and  $\text{MoS}_2$  nano-sheets in  $\text{Graphene}_2(\text{MoS}_2)_1$ . Therefore, micropores (half pore width < 1 nm, pore size < 2 nm) were more pronounced in this combination (Fig. 5c). However, with the excess of graphene, the amount of micropores was deduced as shown in Fig. 5d and e. This was due to the excess graphene with mesopores (3.7 nm).

### 3.4 Diffusion study in lithium-ions storage

To understand the kinetics of lithium ions transport in a  $\text{graphene}_{1-x}(\text{MoS}_2)_x$  electrode, Fig. 6 compared the electrochemical impedance spectroscopy at 50% state of charge (SOC) of the 10th cycle. All the electrodes shown a characteristic linear relation between the real and imaginary parts of the impedance at low frequencies, and a semicircle in the high frequencies, as

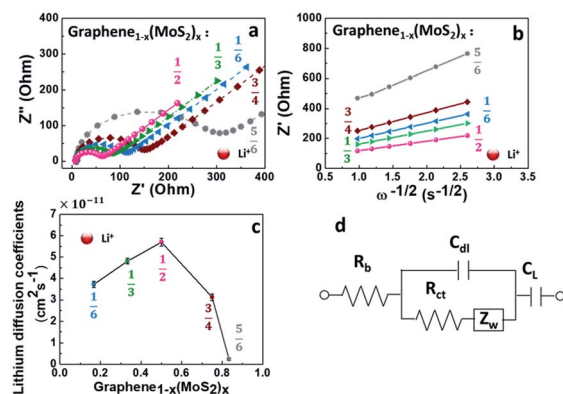


Fig. 6 Electrochemical impedance spectroscopy of  $\text{graphene}_{1-x}(\text{MoS}_2)_x$  electrode in lithium-ion batteries: (a) Nyquist plots, (b) the relationship between  $Z'$  and  $\omega^{-1/2}$  at low-frequency region, (c) lithium diffusion coefficients ( $D_{\text{Li}^+}$ ) at 50% state of charge (SOC) of 10th cycle, (d) equivalent circuit used to model the impedance spectra obtained.  $R_b$  is the equivalent circuit resistance,  $R_{ct}$  is charge-transfer resistance,  $C_{dl}$  is constant phase element which refers to an electric double-layer capacitance on nonhomogeneous systems,  $Z_w$  is the Warburg impedance, which refers to the diffusion of lithium ions in the solid, and  $C_L$  is the intercalation capacitance.

shown in Fig. 6a. The impedance in the low-frequency region corresponds to a Warburg process.<sup>1,13</sup> The impedance at the high-frequency region is related to the lithium-ions migration process. This process corresponds to the charge-transfer resistance  $R_{ct}$  and an electric double-layer capacitance on nonhomogeneous systems  $C_{dl}$ . Here, an equivalent circuit for this model (Fig. 6d) was used to explain the impedance behaviors.<sup>13,30,34,35</sup> As shown in Table 1 and Fig. 6c, with the increase of exfoliated- $\text{MoS}_2$  amount, the  $D_{\text{Li}^+}$  increased and reached a peak when  $x = \frac{1}{2}$  in  $\text{graphene}_{(1-x)}(\text{MoS}_2)_x$ , and then decrease rapidly.  $D_{\text{Li}^+}$  for  $\text{Graphene}_2(\text{MoS}_2)_1$  was  $5.70 \times 10^{-11} \text{ cm}^2 \text{ s}^{-1}$ , which was about twice that of  $\text{Graphene}_4(\text{MoS}_2)_3$ , and about 24 times that of  $\text{Graphene}_6(\text{MoS}_2)_5$ . The value was consistent with the literature.<sup>36</sup> The electrode  $\text{Graphene}_3(\text{MoS}_2)_2$  exhibited the highest lithium-diffusion coefficient, which might be the result of pronounced micropores (<2 nm) shown in Fig. 5c.

Although larger pore size can improve the delivery of ions,<sup>8</sup> pores smaller than 2 nm seem to contribute to the lithium-ion kinetics, as discussed by Li *et al.*<sup>16</sup> and Wang *et al.*<sup>37</sup> It is due to that the micropore can: (1) cause the desolvating of the electrolyte ions,<sup>38</sup> leading to a decrease of dissolution of polysulfide. This is because the concentration of solvent in these micropores is very low compared with that in mesopores. (2) Nearly reversible reaction for sulfur confined in sub-nanometre micropores. However, for the sulfur located in mesopores, the formation of insulation layer on the electrode surface lead to absolute loss of reversibility.<sup>39</sup> (3) Near-perfect confinement level (96.9%) of micropores system compared with other systems with mesopores or micropores.<sup>39,40</sup> This work systematically studied the effect of pore size on lithium-ion diffusion and added experimental evidence to the discussion.

As shown in Fig. 7,  $\text{Graphene}_2(\text{MoS}_2)_1$  exhibited good rate capability. The electrode delivered specific charge capacities of

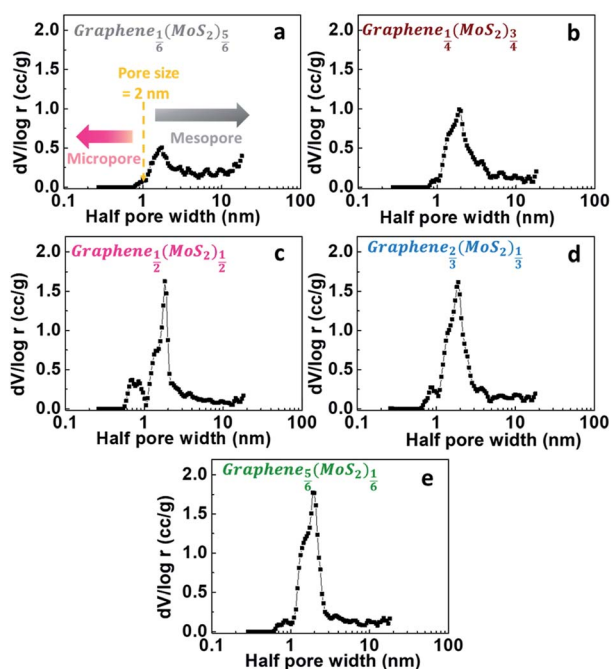


Fig. 5 Pore size distribution curves of (a)  $\text{Graphene}_6(\text{MoS}_2)_5$ , (b)  $\text{Graphene}_4(\text{MoS}_2)_3$ , (c)  $\text{Graphene}_2(\text{MoS}_2)_1$ , (d)  $\text{Graphene}_3(\text{MoS}_2)_2$  and (e)  $\text{Graphene}_5(\text{MoS}_2)_6$ : incremental pore volume as a function of the half pore size calculated from DFT porosity calculations based on data taken from nitrogen gas adsorption measurements.



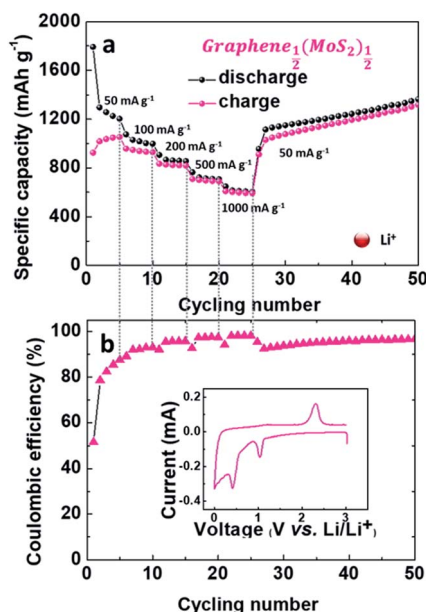


Fig. 7 Electrochemical performance of  $\text{Graphene}_{1/2}(\text{MoS}_2)_{1/2}$  as anode in a lithium-ion battery: (a) rate capability, (b) coulombic efficiency (inset is the cyclic voltammograms (CV) curve in the first cycle at a scan rate of  $0.1 \text{ mV s}^{-1}$ ).

1054.42, 929.29, 819.67, 688.24 and  $592.23 \text{ mA h g}^{-1}$  at current densities of 50, 100, 200, 500 and  $1000 \text{ mA g}^{-1}$ . With the decrease of current density, the specific capacity increased back to  $1030.33 \text{ mA h g}^{-1}$  and slowly increased to  $1319.02 \text{ mA h g}^{-1}$  at the 50th cycle with coulombic efficiency of 97%.

### 3.5 Diffusion study in sodium-ion storage

Although the lithium-ion battery has been greatly developed, the high cost and scarcity of lithium are driving research to develop alternatives to lithium-ion batteries, especially to meet future needs in energy storage. One potential alternative is sodium-ion batteries. Since  $\text{Na}^+$  is about 55% larger than  $\text{Li}^+$ ,<sup>41</sup> a lot of electrode materials in lithium-ion batteries are not suitable in sodium-ion batteries. In this work, the electrochemical performance of  $\text{graphene}_{1-x}(\text{MoS}_2)_x$  in a sodium-ion battery is summarized in Fig. 8.

Fig. 8a depicts Nyquist plots of the impedance of the  $\text{graphene}_{1-x}(\text{MoS}_2)_x$  electrodes in sodium-ion diffusion. The impedance of all the electrodes exhibited a semicircle behavior and a linear behavior in high and low-frequency regions, respectively. The behaviors were similar to those found in lithium-ion diffusion (Fig. 6). As summarized in Table 1, for these electrodes,  $R_{\text{ct}}$  in sodium ions diffusion was larger than that in lithium ions diffusion. This phenomenon was caused by smaller sodium conductivity. The sodium ions diffusion coefficients  $D_{\text{Na}^+}$  for all electrodes were much smaller than lithium ions diffusion coefficient  $D_{\text{Li}^+}$  due to the larger sodium ion radius. Fig. 8c summarizes the sodium diffusion coefficients with the increase of  $\text{MoS}_2$  amount. The  $D_{\text{Na}^+}$  reached a peak,  $9.15 \times 10^{-12} \text{ cm}^2 \text{ s}^{-1}$ , when  $x = \frac{1}{2}$  ( $\text{Graphene}_{1/2}(\text{MoS}_2)_{1/2}$ ), and then decreased to  $2.66 \times 10^{-12} \text{ cm}^2 \text{ s}^{-1}$  and  $0.31 \times 10^{-12} \text{ cm}^2 \text{ s}^{-1}$

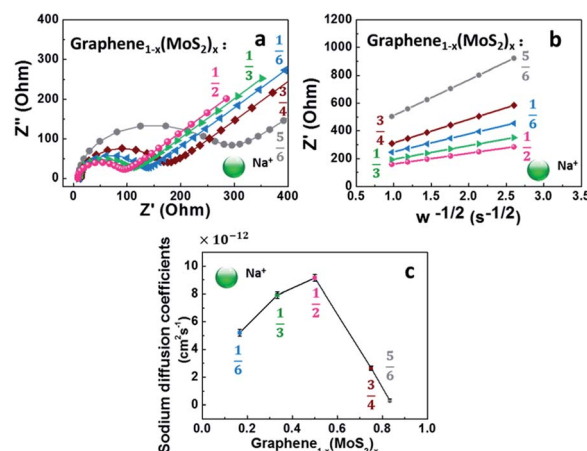


Fig. 8 Electrochemical performance of  $\text{graphene}_{1-x}(\text{MoS}_2)_x$  electrodes in sodium-ion batteries: (a) Nyquist plots, (b) the relationship between  $Z'$  and  $\omega^{-1/2}$  at low frequency region at 50% state of charge (SOC) of 10th cycle, (c) sodium diffusion coefficients ( $D_{\text{Na}^+}$ ).

when  $x$  increased to  $\frac{3}{4}$  and  $\frac{5}{6}$ , respectively. Fig. 9 shows the rate capability of  $\text{Graphene}_{1/2}(\text{MoS}_2)_{1/2}$ . The specific charge capacity was 252.29, 235.24, 206.74, 168.61,  $134.17 \text{ mA h g}^{-1}$  at current densities of 50, 100, 200, 500, and  $1000 \text{ mA g}^{-1}$ . To note that to evaluate the stability of electrode in sodium ions intercalation and de-intercalation, the current density is increased to  $10\,000 \text{ mA g}^{-1}$  ( $10 \text{ A g}^{-1}$ ). The specific charge capacity was  $36.09 \text{ mA h g}^{-1}$ . When the current density decreased back to  $50 \text{ mA g}^{-1}$ , the specific charge capacity of  $\text{Graphene}_{1/2}(\text{MoS}_2)_{1/2}$  was

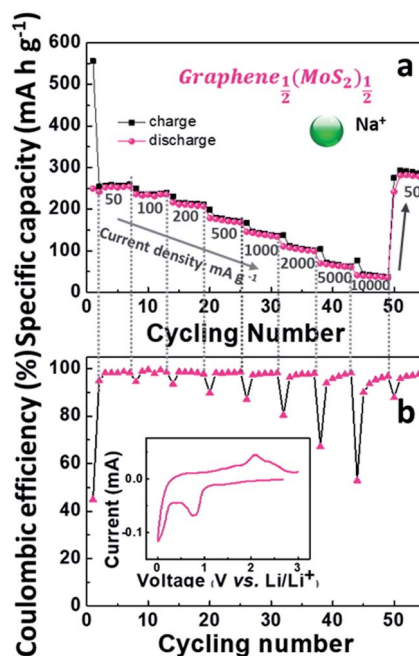


Fig. 9 Electrochemical performance of  $\text{Graphene}_{1/2}(\text{MoS}_2)_{1/2}$  as anode in a sodium-ion battery: (a) rate capability, (b) coulombic efficiency (inset is the cyclic voltammograms (CV) curve in the first cycle at a scan rate of  $0.1 \text{ mV s}^{-1}$ ).





282.37 mA g<sup>-1</sup> (coulombic efficiency: 96%), indicating the stability of this electrode.

## 4. Conclusions

In this work, we studied the performance of micro-mesoporous graphene<sub>1-x</sub>(MoS<sub>2</sub>)<sub>x</sub> as anode in lithium-ion and sodium-ion batteries. We show that although large specific surface area provides more active sites to contact with electrolyte, it leads to increase of the irreversible capacity during the formation of solid electrolyte interphase. The pore size distributions of all micro-mesoporous graphene<sub>1-x</sub>(MoS<sub>2</sub>)<sub>x</sub> samples appear to be similar, with the averaged pore size being about 3.7 nm. The lithium diffusion coefficient of Graphene<sub>2/3</sub>(MoS<sub>2</sub>)<sub>1/3</sub> electrode with pronounced micropores smaller than 2 nm is about twice that of Graphene<sub>3/4</sub>(MoS<sub>2</sub>)<sub>1/4</sub> with scanty micropores. Graphene<sub>2/3</sub>(MoS<sub>2</sub>)<sub>1/3</sub> achieves a specific charge capacity of 1319.02 mA h g<sup>-1</sup> at the 50th cycle in lithium ion batteries. The discussion in this work may provide a clue of electrode material structural design.

## Conflicts of interest

There are no conflicts to declare.

## Acknowledgements

This work was supported by NIMS microstructural characterization platform as a program of "Nanotechnology Platform" of the Ministry of Education, Culture, Sports, Science and Technology (MEXT), Japan. Da-Ming Zhu is supported by a Funding for Excellence grant from University of Missouri-Kansas City and by a University of Missouri Research Board grant.

## References

- 1 M. Wakihara and O. Yamamoto-Weinheim, *Lithium Ion Batteries: Fundamentals and Performance*, Wiley-VCH, Berlin, New York, Chichester, Brisbane, Singapore, Toronto, 1998.
- 2 X.-X. Yuan, H.-S. Liu and J.-J. Zhang, *Lithium-ion Batteries: Advanced Materials and Technologies*, CRC Press, Boca Raton, London, New York, 2011.
- 3 J. B. Goodenough and K.-S. Park, *J. Am. Chem. Soc.*, 2013, **135**, 1167–1176.
- 4 J. B. Goodenough and Y. Kim, *Chem. Mater.*, 2010, **22**, 587–603.
- 5 Y. Li, B. Xu, H. Xu, H. Duan, X. Lü, S. Xin, W. Zhou, L. Xue, G. Fu, A. Manthiram and J. B. Goodenough, *Angew. Chem.*, 2017, **129**, 771–774.
- 6 Y. Ren, L. J. Hardwick and P. G. Bruce, *Angew. Chem., Int. Ed.*, 2010, **49**, 2570–2574.
- 7 J.-Y. Luo, J.-J. Zhang and Y.-Y. Xia, *Chem. Mater.*, 2006, **18**, 5618–5623.
- 8 A. D. Roberts, X. Li and H. Zhang, *Chem. Soc. Rev.*, 2014, **43**, 4341–4356.
- 9 Y.-P. Wu, C.-R. Wan, C.-R. Wan, C.-Y. Jiang, S.-B. Fang and Y. Y. Jiang, *Carbon*, 1999, **37**, 1901–1908.
- 10 B. Fang, M.-S. Kim, J. H. Kim, S. Lim and J.-S. Yu, *J. Mater. Chem.*, 2010, **20**, 10253–10259.
- 11 T. Takamura, H. Awano, T. Ura and K. Sumiya, *J. Power Sources*, 1997, **68**, 114–119.
- 12 F. Joho, B. Rykart, A. Blome, P. Novák, H. Wilhelm and M. E. Spahr, *J. Power Sources*, 2001, **97–98**, 78–82.
- 13 V. Ramar, K. Saravanan, S. R. Gajjela, S. Hariharan and P. Balaya, *Electrochim. Acta*, 2013, **105**, 496–505.
- 14 P. Novák, F. Joho, M. Lanz, B. Rykar, J.-C. Panitz, D. Allia, R. Küta and O. Haas, *J. Power Sources*, 2001, **97–98**, 39–46.
- 15 D. Saikia, T.-H. Wang, C.-J. Chou, J. Fang, L.-D. Tsai and H.-M. Kao, *RSC Adv.*, 2015, **5**, 42922–42930.
- 16 J. Li, L. Wang, X. He and J. Wang, *ACS Sustainable Chem. Eng.*, 2016, **4**, 4217–4223.
- 17 Y. Jeong, K. Lee, K. Kim and S. Kim, *Materials*, 2016, **9**, 995.
- 18 T. Dominko, J. M. Goupil, M. Bele, M. Gaberscek, M. Remskar, D. Hanzel and J. Jamnik, *J. Electrochem. Soc.*, 2005, **152**, A858–A863.
- 19 H. Yu, C. Ma, B. Ge, Y. Chen, Z. Xu, C. Zhu, C. Li, Q. Ouyang, P. Gao, J. Li, C. Sun, L. Qi, Y. Wang and F. Li, *Chem.-Eur. J.*, 2013, **19**, 5818–5823.
- 20 W. Fang, C. Hua, X. Guo, Y. Hu, Z. Wang, X. Gap, F. Wu, J. Wang and L. Chen, *Electrochim. Acta*, 2012, **81**, 155–160.
- 21 T. S. Saha and S. Mitra, *Sci. Rep.*, 2015, **5**, 12571.
- 22 C. Zhai, N. Du, H. Zhang, J. Yu, P. Wu, C. Xiao and D. Yang, *Nanoscale*, 2011, **3**, 1798–1803.
- 23 J. Jamnik and J. Maier, *Phys. Chem.*, 2003, **5**, 5215–5218.
- 24 Y. S. Su and A. Manthiram, *Chem. Commun.*, 2012, **48**, 8817–8823.
- 25 Y. Xu, Y. Huang, W. Yan, L. Zhang and Y. Chen, *J. Nanosci. Nanotechnol.*, 2013, **13**, 1116–1119.
- 26 X. Cao, Y. Shi, W. Shi, X. Rui, Q. Yan, J. Kong and H. Zhang, *Small*, 2013, **9**, 3433–3438.
- 27 Y. Sun, J. Tang, K. Zhang, J. Yuan, J. Li, D.-M. Zhu, K. Ozawa and L.-C. Qin, *Nanoscale*, 2017, **9**, 2585–2595.
- 28 Q. Cheng, J. Tang, J. Ma, H. Zhang, N. Shinya and L.-C. Qin, *Phys. Chem. Chem. Phys.*, 2011, **13**, 17615–17624.
- 29 X. Wang, H. Hao, J. Liu, T. Huang and A. Yu, *Electrochim. Acta*, 2011, **56**, 4065–4069.
- 30 Y. Sun, C. Xu, B. Li, J. Zao, Y. He, H. Du and F. Kang, *Int. J. Electrochem. Sci.*, 2014, **9**, 6387–6401.
- 31 S. Lowerll and J. E. Shields, *Powder surface area and porosity*, Chapman & Hall, 3rd edn, New York, 1991.
- 32 J. C. Groen, L. A. A. Peffer and J. Pérez-Ramírez, *Micropor. Mesopor. Mat.*, 2003, **60**, 1–17.
- 33 T. Stephenson, Z. Li, B. Olsen and D. Mitlin, *Energy Environ. Sci.*, 2014, **7**, 209–231.
- 34 K. Dokko, M. Mohamedi, Y. Fujita, T. Itoh, M. Nishizawa, M. Umeda and I. Uchida, *J. Electrochem. Soc.*, 2001, **148**, A422–A426.
- 35 L. Wang, J. Zhao, X. He, J. Gao, J. Li, C. Wang and C. Jiang, *Int. J. Electrochem. Sci.*, 2012, **7**, 345–353.
- 36 M. A. S. Ana, E. Benavente, P. Gómez-Romero and G. González, *J. Mater. Chem.*, 2006, **16**, 3107–3113.
- 37 D.-W. Wang, Q. Zeng, G. Zhou, L. Yin, F. Li, H.-M. Cheng, I. T. Gentle and G. Q. M. Lu, *J. Mater. Chem. A*, 2013, **1**, 9382–9394.



- 38 J. Chmiola, G. Yushin, Y. Gogotsi, C. Portet, P. Simon and P. L. Taberna, *Science*, 2006, **313**, 1760–1763.
- 39 S.-E. Cheon, K.-S. Ko, J.-H. Cho, S.-W. Kim, E.-Y. Chin and H.-T. Kim, *J. Electrochem. Soc.*, 2003, **150**, A800–A805.
- 40 G. Zhou. *Design, Fabrication and electrochemical performance of nanostructured carbon based materials for high-energy lithium-sulfur batteries*, Springer Singapore, Singapore, 2017.
- 41 D. A. Stevens and J. R. Dahn, *J. Electrochem. Soc.*, 2001, **148**, A803–A811.

